Journal of
Materials Chemistry A

ROYAL SOCIETY OF CHEMISTRY

Reduced graphene oxide supported AgxNi100-x alloy nanoparticles: A highly active and reusable catalyst for the reduction of nitroarenes

SCHOLARONE™
Manuscripts

Reduced graphene oxide supported Ag_xNi_{100-x} alloy nanoparticles: A highly active and reusable catalyst for the reduction of nitroarenes

Ritu Dhanda, Mazaahir Kidwai[*]

Green chemistry research laboratory, Department of Chemistry, University of Delhi, North campus, New Delhi-110007, India

Abstract. The synthesis of supported, small sized, monodisperse, surfactant free bimetallic nanoparticles (NPs) is of great importance in the field of catalysis. In this paper, we report a facile and green method to synthesize Ag_xNi_{100-x} (x = 25, 50, 75, 100) alloy NPs decorated on reduced graphene oxide (RGO) nanosheets by in situ chemical co-reduction process for the first time. The resulting products were well characterized using X-ray diffraction (XRD), Fourier transform infrared spectroscopy (FTIR), Raman spectroscopy, energy dispersive X-ray spectroscopy (EDS), transmission electron microscopy (TEM), high resolution TEM (HRTEM), X-ray photoelectron microscopy (XPS) and inductively coupled plasma atomic absorption spectroscopy (ICP-AES). The insitu synthesized Ag_xNi_{100-x}/RGO alloy nanocomposites showed remarkable composition dependent catalytic activity towards the reduction of 4-nitrophenol by $NaBH_4$ with one of the best activity parameter ($968 \ s^{-1}g^{-1}$). The enhanced catalytic performance was observed for RGO supported NPs as compared to bare AgNi alloy NPs and the insitu synthesized $Ag_{50}Ni_{50}$/RGO sample was identified to be highest active among the as obtained nanocomposite samples. $Ag_{50}Ni_{50}$/RGO sample catalyzed the reduction of other nitroarenes in such a way that we got ever best activity parameter for those reactions also. Furthermore, effect of support materials (activated carbon, SBA-15 or RGO) and reducing agent (ammonia borane or sodium borohydride) was studied on catalytic activity of $Ag_{50}Ni_{50}$ alloy NPs. In addition, Ag_xNi_{100-x}/RGO nanocomposite showed excellent recycling stabilities which may lead to the use of present nanocatalyst in many more industrially important catalytic applications.

Keywords: AgNi alloy nanoparticles; reduced graphene oxide; nanocomposites; 4-nitrophenol.

1. Introduction

Graphene, a monolayer of sp^2 carbon network has attracted intense scientific interest owing to its high conductivity (10^5-10^6 Sm^{-1}), large surface area (2000-3000 m^2g^{-1}), low manufacturing cost and exceptional mechanical, optical, thermal and magnetic properties.[1-3] With these advantages, graphene can act as a most promising catalyst support for use in various fields like sensors,[4] electronics,[5] electrochemical energy storage,[6] efficient catalysis[7] etc. In general, graphene nanocomposites can be prepared in large scale via oxidative exfoliation of

common graphite to graphene oxide (GO) and the subsequent chemical or thermal reduction to RGO sheets.[8] Recently various metals[9,10] and metal oxides[11,12] NPs were decorated on graphene nanosheets via co-reduction of metal salts and graphene oxide in one pot manner which showed enhanced properties and improved functionalities due to synergistic effect between NPs and graphene nanosheets. Moreover, NPs can also act as a spacer between graphene nanosheets to minimize the agglomeration of them.[13]

Most recently, transition metals and their bimetallic alloy nanostructures have attracted considerable attention owing to their composition dependent excellent and unique optical, electronic, magnetic and catalytic properties which led to the use of these nanostructures in diverse areas such as catalysis,[14,15] optics,[16] electronics[17] and biomedicine.[18] Among various bimetallic systems, AgNi alloy represents one of the most important class due to unique combination between noble and non-noble metals. Among noble metals, Ag is particularly attractive due to high electrical conductivity, antibacterial activity and relatively low cost as compared to other noble metals. Introduction of magnetic Ni atoms in Ag crystal lattice further enhance its activity by synergistic effect and also make AgNi alloy as cost effective and magnetically separable nanocatalyst. From literature survey, we found phase segregated core@shell structure as the most thermo-dynamically favorable for AgNi NPs because of the lower surface energy of Ag, 14% lattice mismatch and complete immiscibility in phase diagram.[19-21] However at Nano level, surface effects and the alloy composition favor alloy formation with better phase stability by changing the heat of formation from positive to negative.[22] In recent years, various approaches such as molecular beams, thermal decomposition of transition metal complexes, radiolysis, γ-radiation technique, electrochemical synthesis and chemical reduction have been reported for the synthesis of binary AgNi alloy NPs.[23-29] However, to the best of our knowledge no work has been done earlier on surfactant free RGO supported Ag_xNi_{100-x} alloy NPs.

In this paper we present a facile, aqueous, low temperature simultaneous chemical reduction method for the synthesis of Ag_xNi_{100-x} alloy NPs on RGO nanosheets for the first time. In this synthesis process, $NaBH_4$ reduced the Ag^+ and Ni^{2+} precursors in presence of GO resulting into Ag_xNi_{100-x}/RGO where GO sheets provide nucleation sites for alloy NPs growth. Ag_xNi_{100-x}/RGO nanocomposites were characterized by XRD, FTIR, Raman, TEM, HRTEM,

EDS and XPS. The catalytic activity and stability of nanocomposites was investigated by reduction of nitroarenes with $NaBH_4$ using time dependent UV-Vis absorption spectroscopy. Nitroarenes are very important for industries and pharmaceuticals[10] but at the same time they contribute to major class of environment pollutants.[30,31] Hence to reduce these hazardous nitro compounds into beneficial amine, various nanomaterials have been developed so far. Due to high density, monodisperse and small size, AgNi alloy NPs loaded on GO nanosheets exhibit the superior catalytic activity towards nitroarenes reduction reaction as compared to few of the best activities reported recently.

2. Experimental

2.1. Chemicals and materials: Silver nitrate ($AgNO_3$, 99.9%), 3-nitroaniline (3-NA), 4-nitroaniline (4-NA), 2-nitroaniline (2-NA), 2-nitrophenol (2-NP) and 4-nitrophenol (4-NP) were from Sisco-chem Industries, Bombay, India. SBA-15 was purchased from SRL India. 2-amino-4-nitrophenol (ANP), 4-flouro-3-nitroaniline (FNA) was from Thomas Baker chemicals Pvt. limited. Sodium borohydride ($NaBH_4$, 96%), were from Spectrochem Pvt. Ltd. India. Nickel nitrate hexahydrate ($NiNO_3.6H_2O$, 98.5%) was from Merck India. Natural flake graphite and ammonia borane complex (97%, AB) were purchased from Sigma Aldrich India. Activated carbon powder was purchased from Qualikems fine chemicals Pvt. Ltd. India. All chemicals were used as received without any further purification. Deionized water was used in all experiments. GO was synthesized from natural graphite powder according to improved Hummers method.[8]

2.2. Preparation of Ag_xNi_{100-x} alloy nanoparticles on RGO nanosheets: The typical procedure for synthesis RGO attached $Ag_{50}Ni_{50}$ alloy NPs is as follows: 40 mg of GO was dispersed in 30 ml of water via ultra-sonication. Subsequently, 0.15 mmol of $NiNO_3.6H_2O$ and 0.15 mmol $AgNO_3$ (molar ratio of Ag:Ni = 1:1) was dissolved in 10 ml of water and then gradually added to the GO dispersion. The resulting reaction mixture was magnetically stirred for 10 minutes and N_2 was passed to purge out all dissolved oxygen. Then freshly prepared $NaBH_4$ (8 ml, 1.0 M) was added drop wise to the reaction mixture under N_2 atmosphere. The whole setup was maintained at room temperature and stirred for 30 minutes under N_2 blanket. Then resulted

mixture was refluxed at 110 ^{o}C for next 2.5 h. The resulted black product was isolated by centrifugation, washed with water for three times and then dried in oven at 50 ^{0}C. Similar scheme was applied for synthesis of Ag/RGO, $Ag_{75}Ni_{25}$/RGO, and $Ag_{25}Ni_{75}$/RGO samples by adjusting the molar ratios of Ag/Ni precursors. Detailed parameters for synthesis of all nanocomposite samples are shown in Table 1. For comparison, bare $Ag_{50}Ni_{50}$ alloy NPs were also synthesized using similar procedure without the addition of GO.

2.3. In-situ synthesis of activated carbon or SBA-15 supported $Ag_{50}Ni_{50}$ alloy NPs: Similar synthesis protocols were followed for synthesis of activated carbon or SBA-15 supported alloy NPs as followed in synthesis of Ag_xNi_{100-x} /RGO nanocomposites except addition of activated carbon or SBA-15 in place of GO.

2.4. Exsitu synthesis of activated carbon and RGO supported $Ag_{50}Ni_{50}$ alloy NPs: RGO was synthesized similar to insitu Ag_xNi_{100-x}/RGO nanocomposites except addition of Ag^+ and Ni^{2+} precursors. For synthesis of exsitu activated carbon or RGO supported $Ag_{50}Ni_{50}$ NPs, 9 mg of previously synthesized bare $Ag_{50}Ni_{50}$ alloy was mixed in 25 mg of activated carbon or RGO sheets and sonicated for 4h. The calculated percentage loading for $Ag_{50}Ni_{50}$ was 26%.

2.3. Characterization: The phase purity and crystal structure of synthesized samples were examined using X-ray diffraction (XRD, Bruker D8 Advance diffractomer) with Cu Kα as a radiation source ($\lambda = 1.5406$ Å) at a scanning rate of 4° min^{-1}. TEM and HRTEM images were obtained from Phillips Technai G^{2}30 transmission electron microscope operating at 200 kV accelerating voltage. TEM samples were prepared by putting a drop of sample dispersion in ethanol on carbon coated copper grid and allowing the solvent to evaporate at room temperature. Elemental compositions of alloy samples were determined by EDS and ICP-AES. EDS was recorded on energy dispersive spectrometer attached with JEOL JSM-6610LV scanning electron microscope (SEM). ICP-AES was done using ARCOS system from M/s. Spectro, Germany. The X-ray photoelectron spectroscopy measurement was performed using SPECS XPS system. Magnetic properties of Ag_xNi_{100-x} nanocomposite samples were measured by vibrating sample magnetometer (MicroSense EV9) at room temperature (20±1 ^{o}C). Raman study was done using Renishaw inVia Raman spectrometer equipped with a laser having a wavelength of 514 nm. Fourier transform infrared (FTIR) spectra (KBr disk, 4000−400 cm^{-1}) were recorded on a Perkin

Elmer FT-IR 2000 spectrophotometer. Optical absorption spectra were recorded using Analytikjena 250 UV-Vis spectrophotometer.

2.4. Catalytic reduction of nitro-aromatic compounds: The catalytic activity of present nanocatalysts was evaluated using aromatic nitro compounds reduction reactions as a model system. In a typical procedure, 1.8 mL of aqueous solution of 4-NP (0.25 mM) and 0.5 mL of 0.1 M $NaBH_4$ was taken in a standard quartz cuvette of 1 cm length and 3 mL volume. After that, 0.1 mL of aqueous dispersion of as synthesized nanocatalyst (0.05 mg, 0.5 mg/mL) was added in same cuvette and UV-Vis absorption spectra were recorded immediately at room temperature. Similar reaction procedure was applied for evaluating catalytic activity of insitu RGO supported Ag, $Ag_{25}Ni_{75}$, $Ag_{50}Ni50$ and $Ag_{75}Ni_{25}$ samples. For catalytic study of insitu synthesized activated carbon or SBA-15 supported $Ag_{50}Ni_{50}$ alloy NPs, 0.3 mL (0.15 mg, 0.5 mg/mL) of aqueous dispersion of nanocatalyst was used under similar catalytic reaction while for studying reaction kinetics of exsitu synthesized RGO or activated carbon supported $Ag_{50}Ni_{50}$ alloy NPs, 0.5 mL (0.25 mg, 0.5 mg/mL) of aqueous dispersion of nanocatalyst was used. Reduction of other nitro derivatives was studied using highest active insitu $Ag_{50}Ni_{50}$/RGO nanocomposites following similar reaction procedure as for 4-NP reduction.

2.4. Tandem catalytic reduction of nitro-aromatic compounds: In a typical procedure, 5.4 mL of aqueous solution of nitro compound (0.25 mM) and 1.5 mL of 0.1 M AB was taken in a vial. After that 1 mL of aqueous dispersion of highest active insitu $Ag_{50}Ni_{50}$/RGO nanocatalyst (0.5 mg, 0.5 mg/mL) was added in same vial and UV-Vis absorption spectra were recorded after regular time interval at room temperature.

3. Result and discussion

3.1 Characterization of Ag_xNi_{100-x} alloy nanocomposites

The phase purity, composition of alloy NPs and successive reduction of GO was examined by XRD measurement. Figure 1 display the XRD patterns of GO, Ag/RGO, bare $Ag_{50}Ni_{50}$ and all Ag_xNi_{100-x}/RGO alloy samples. From XRD spectrum it was found that, GO exhibit two peaks centered at $2\theta = 9.94°$ and $42.4°$ corresponding to its (001) and (002) planes.[8]

However, these XRD peaks was not observed in RGO supported NPs indicating complete reduction of GO to RGO nanosheets. Moreover a small hump centered at $2\theta = 24^\circ$ corresponding to (002) reflection of RGO nanosheets was not clearly seen for nanocomposite samples which may be due to high intense metal peaks over RGO nanosheets.[10] The diffraction pattern of Ag/RGO sample exhibit five characteristic peaks centered at $2\theta = 38.10^\circ$, 44.31°, 64.52°, 77.39° and 81.62° corresponding to the (111), (200), (220), (311) and (222) plane of face centered cubic (*fcc*) structure of Ag bulk state (JCPDS NO. 04-0783). Similarly RGO supported Ag_xNi_{100-x} alloy NPs also exhibit five characteristic peaks with slight deviation from actual 2θ values as compared to pure Ag/RGO sample. The peak corresponding to (200) plane of Ag_xNi_{100-x}/RGO nanocomposites lies between pure Ag (200) and pure Ni (111) peaks and move towards Ni (111) peak with increasing Ni content which indicate decrease in lattice constant value for alloy NPs with increasing Ni molar ratio. This was obviously due to substitution of larger sized Ag atoms (144 pm) with smaller Ni atoms (124 pm) from silver matrix. XRD pattern of insitu synthesized activated carbon or SBA-15 supported $Ag_{50}Ni_{50}$ alloy NPs also exhibit five characteristics peak of AgNi alloy NPs representing pure phase synthesis of these nanocomposites (figure S1). For different alloy compositions, no peak was observed at $2\theta = 52.15^\circ$ corresponding to (200) plane of *fcc* Ni metal which eliminates all the possibility of heterogeneous Ni NPs.[26-29] The resemblance with Ag *fcc* structure and absence of characteristic Ni peak indicates that Ni atoms grow only inside the Ag lattice and form a solid solution. This fact was further supported from detailed study of XRD spectrum of $Ag_{25}Ni_{75}$/RGO and pure Ni/RGO samples (Figure S1). XRD spectrum of $Ag_{25}Ni_{75}$/RGO samples not only represents characteristic Ag fcc structure but also contains some impurity peaks corresponding to $Ni(OH)_2$ (JCPDS card 22–0752) which may be due to oxidation of excess of Ni metal atom which was not accommodated by Ag lattice since initial Ag/Ni are in 1:3 ratio. However no such oxidation was observed for $Ag_{75}Ni_{25}$/RGO and $Ag_{50}Ni_{50}$/RGO samples where Ag/Ni molar ratio is 3:1 and 1:1 respectively. For further study pure Ni/RGO nanocomposite was synthesized which again showed characteristic peaks corresponding to α-$Ni(OH)_2$, however no metallic Ni was observed in XRD spectrum of pure Ni/RGO. As above discussed results conclude that Ni(0) atoms are not stable in absence of Ag lattice and get easily oxidized, however presence of balanced Ag stabilize the Ni(0) atoms by providing nucleation sites and hence prevent oxidation.
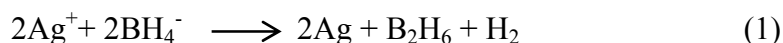
The effective reduction of GO to RGO and successful synthesis of RGO supported $Ag_{50}Ni_{50}$ alloy nanoparticles can be further explained by the FTIR, Raman and XPS studies. Figure 2a represents the FTIR spectra of GO and $Ag_{50}Ni_{50}$/RGO samples. The FTIR spectrum of GO clearly shows the presence of numerous oxygen containing groups. For GO the broad absorption at 3429 cm^{-1} can be assigned as O-H stretching vibration. The other peaks at 1724, 1394 and 1120 cm^{-1} appears due to C=O stretching mode, O-H bending mode and C-O (alkoxy) stretching mode. Peaks centered at 2860 and 2928 cm^{-1} in the spectrum of GO also remain prominent in $Ag_{50}Ni_{50}$/RGO can be assigned to $-CH_2$ stretching vibrations of graphene sheets. The peak at 1629 cm^{-1} in GO can be assigned to the vibration of absorbed water molecule on graphene oxide sheets.[32] However FTIR spectrum of $Ag_{50}Ni_{50}$/RGO sample show a decrease in absorption intensity for O-H group (3429 cm^{-1}) and absence of absorption peak corresponding to C=O (1724 cm^{-1}), C-O (1126 cm^{-1}) stretching vibrations. The absence of peak at 1629 cm^{-1} indicates removal of adsorbed water molecules from GO sheets during synthesis of $Ag_{50}Ni_{50}$/RGO nanocomposites. These results clearly indicate that GO has been reduced upto a great extent. A new absorption peak at 1560 cm^{-1} in case of $Ag_{50}Ni_{50}$/RGO nanocomposite can be assigned to skeletal vibration of RGO sheets.

Raman spectroscopy is a powerful tool in characterization of structural properties of carbon based materials. Figure 2b represents the Raman spectra of GO and $Ag_{50}Ni_{50}$/RGO nanocomposite samples. As shown in Raman spectrum, GO display two prominent peaks at 1356 cm^{-1} and 1601 cm^{-1} corresponding to D and G band of carbon respectively while small shifting was observed in D and G bands of $Ag_{50}Ni_{50}$/RGO sample indicating increase in randomness and removal of oxygen containing functional groups from graphene oxide sheets. It is well known that D band can be assigned to disordered structure or defects in graphene nanosheets while G band is associated with E_{2g} mode observed for sp^2 carbon domains.[33] The intensity ratio of D and G band (I_D/I_G) for $Ag_{50}Ni_{50}$/RGO sample (I_D/I_G = 1.26) shows enhanced value as compared to GO (I_D/I_G = 0.82) which suggests that conjugated graphene network (sp^2) is re-established after chemical reduction resulting increased I_D/I_G value for $Ag_{50}Ni_{50}$/RGO nanocomposite.[10]

The size, morphology and crystal structure of Ag_xNi_{100-x}/RGO nanocomposites were further studied by TEM and HRTEM. The low resolution TEM images for pure Ag/RGO and Ag_xNi_{100-x}/RGO nanocomposites are shown in Figure 3a-d. In all cases, it was observed that as

synthesized Ag and Ag_xNi_{100-x} alloy NPs are uniformly dispersed on RGO nanosheets without obvious agglomeration. The NPs were not observed outside the RGO nanosheets indicating very good interactions between nanoparticles and RGO nanosheets (more TEM images in Figure S2). The average particle size for pure Ag NPs supported on RGO nanosheets was found to be ~17±3 nm whereas a little smaller size was observed for all alloy compositions (Figure 3e-h). The average particle size for $Ag_{75}Ni_{25}$, $Ag_{50}Ni_{50}$ and $Ag_{25}Ni_{75}$ alloy nanoparticles is about ~10±3 nm, ~11±3 nm and ~14±3 nm respectively. The decrease in size of AgNi alloy NPs over pure Ag NPs is obviously due to replacement of larger Ag (144 pm) atoms with small sized Ni (124 pm) atoms from Ag matrix. Figure 4a-d represents the low resolution TEM images for insitu AgNi/C, insitu AgNi/SBA-15, exsitu AgNi/C and exsitu AgNi/RGO nanocomposites. In exsitu synthesis, bare AgNi alloy NPs were synthesized earlier and then supported on activated carbon or RGO sheets via ultra-sonication. Since bare AgNi alloy NPs are not stable so that NPs gets aggregated and form agglomerated AgNi alloy NPs on support material while in case of insitu synthesized AgNi/C and AgNi/SBA-15 nanocomposites AgNi alloy NPs were found homogeneously distributed only on support material. For further study, HRTEM analysis was done on $Ag_{50}Ni_{50}$/RGO sample which reveals crystalline structure of as synthesized RGO supported $Ag_{50}Ni_{50}$ alloy NPs. The interplaner spacing (d_{hkl}) was calculated from adjacent lattice fringes was found to be 0.234 nm which can be indexed to (111) plane of *fcc* AgNi alloy nanocrystals (Figure 5a). The two dimensional fast-fourier transform (2D-FFT) pattern calculated for $Ag_{50}Ni_{50}$/RGO sample is shown in Figure 5b also confirmed the exposure of (111) plane for AgNi alloy nanocrystals. The elemental analysis was carried out on all alloy compositions using EDS and obtained results were shown in Figure 5c and Figure S3. The EDS results confirmed the presence of Ag, Ni, C and oxygen in all samples. The Ag/Ni ratio obtained from EDS was found to be consistent with stoichiometric elemental ratios for all alloy compositions. The carbon element detected in EDS would come from RGO nanosheets while oxygen represents residual oxygen containing functional groups on RGO nanosheets. The actual elemental composition and percentage loading for Ag_xNi_{100-x}/RGO nanocomposites were further analyzed by ICP-AES study. The results are given in Table 1. The Ag/Ni molar ratio calculated from ICP study was found near to initial precursor ratio which again confirmed the controlled synthesis of alloy nanocomposites.

Ag$_x$Ni$_{100-x}$ /RGO formation mechanism: When Ag$^+$ and Ni^{2+} precursors were mixed with the GO dispersion, some Ag$^+$ and Ni^{2+} ions would attach to GO via electrostatic interaction between positively charged metal ions and negatively charged oxygen containing functional groups of GO sheets. After introduction of reductant NaBH$_4$, Ag$^+$ and Ni^{2+} ions reduces rapidly to their metallic state and grow to form alloy nanostructures. During this GO also reduces to RGO nanosheets. Since redox potential of Ag$^+$/Ag (0.8 V) is high over Ni^{2+}/Ni (-0.246V) hence reduction of Ag$^+$ ions occurs in initial phase followed by Ni^{2+} ions. From XRD results, it was observed that metallic nickel atoms are not stable in absence of Ag lattices; however presence of balanced Ag/Ni precursors resulted into formation of stable alloy nanoparticles (In case of Ag$_{75}$Ni$_{25}$/RGO and Ag$_{50}$Ni$_{50}$/RGO). It was also found that Ag$_{25}$Ni$_{75}$/RGO nanocomposite sample exhibits impurity in XRD results due to oxidation of excess nickel which was not accommodated by Ag lattice. These experimental observations indicated that Ag metal ion might reduce earlier than Ni^{2+} ion and provided lattice sites for Ni^0 atoms nucleation and stabilize them. The chemical reaction involved in reduction procedure can be expressed as follows[27]:

$$2Ag^+ + 2BH_4^- \longrightarrow 2Ag + B_2H_6 + H_2 \qquad (1)$$

$$Ni^{2+} + 2BH_4^- \longrightarrow Ni^0 + B_2H_6 + H_2 \qquad (2)$$

$$GO + 2BH_4^- \longrightarrow RGO + B_2H_6 + H_2 \qquad (3)$$

The elemental composition and surface oxidation state of Ag$_{50}$Ni$_{50}$/RGO nanocomposites were further examined by XPS .The survey spectrum reveals that the Ag$_{50}$Ni$_{50}$/RGO nanocomposites contain C, O, Ag and Ni as the main elements (Figure 6a). For further investigation high resolution XPS of C 1s, Ag 3d and Ni 2p were done as displayed in Figure 6b-d respectively. High resolution deconvoluted C 1s spectrum display four peaks centered at 284.5, 286.3, 288.2 and 289.3 eV corresponding to C-C/C=C/C-H, C-OH, C=O and O=C-O bonds of sp^2 carbon of RGO respectively.[8] For C 1s spectrum, high intensity of C-C/C=C/C-H peak was observed over C-OH, C=O and O=C-O peaks indicating reduction of GO.[11] The Ag 3d core level spectrum show Ag 3d$_{5/2}$ and Ag 3d$_{3/2}$ peaks centered at 367.5 and 373.5 eV with a difference of 6 eV indicating metallic Ag in Ag$_{50}$Ni$_{50}$/RGO hybrid[27-29] whereas Ni 2p$_{3/2}$ and Ni 2p$_{1/2}$ peaks appear at 853.3 and 871 eV respectively which is also in good agreement with zero valence Ni atoms in AgNi alloy NPs.[34] From literature survey it was found that RGO supported Ag NPs

exhibit binding energy peak at ~0.5±0.2 eV higher than pure unsupported Ag metal which can be due to interaction with graphene sheets[35], while in our case Ag 3d peaks come near to pure metal (367.5 and 373.5 eV) which may be due electronic interactions between electro-negatively different Ag and Ni metals which is obvious for alloy materials. This fact was further supported by higher value of Ni 2p peaks (853.3 and 871 eV) compared to pure Ni metal again indicating electronic interactions between Ag and Ni metals.[27,34]

3.2 Magnetic properties

Magnetic properties of as synthesized nanocomposites were investigated at room temperature (20±1 °C) using a vibrating sample magnetometer with an applied magnetic field of -22000 Oe to 22000 Oe. The hysteresis loops for all alloy compositions were shown in Figure 6e,f which clearly reveals weak ferromagnetic behavior for alloy nanocomposites owing to presence of Ni metal. The values of saturation magnetization (M_s), remanent magnetization (M_r) and coercivity (H_c) were measured for all alloy compositions and entered in Table 2. As mentioned, the M_s values of Ag_xNi_{100-x}/RGO nanocomposites increase with increase in Ni content which is consistent for AgNi alloy nanostructures.[27,29] However decrease in M_r and H_c values was observed with increasing Ni content which indicated deviation in magnetic behavior from weak ferromagnetic to superparamagnetic.

3.3. Catalytic reduction of nitroarenes

To evaluate the catalytic activity of the synthesized nanocatalyst samples, reduction of 4-NP by $NaBH_4$ was chosen as a first model reaction that can be monitored by time dependent UV-Vis spectroscopy. The aqueous solution of 4-NP is light yellow in colour and show strong absorption at 317 nm. After addition of $NaBH_4$, colour change was observed from light yellow to deep yellow and a strong absorption peak at 400 nm appears due to formation of 4-nitrophenolate ion.[36] Further in blank test, no change in absorption intensity was observed for a long time with $NaBH_4$, which indicate reduction reaction does not occur without addition of catalyst. After addition of catalyst, absorption peak at 400 nm due to 4-nitrophenolate ions gradually decreases and at the same time a new peak start rising at 300 nm indicating formation of 4-aminophenol from 4-nitrophenolate ion (Figure 7a-e). It should be noted that $Ag_{50}Ni_{50}$/RGO sample showed the highest activity and finishes the reaction in just 60 s while a little more time

was observed for all other nanocatalyst samples. Bare $Ag_{50}Ni_{50}$ sample showed lowest activity and took around 10 min for completion of reduction reaction. The poor catalytic performance of bare $Ag_{50}Ni_{50}$ alloy NPs compared to nanocomposites indicate significant role of RGO nanosheets in enhancement of catalytic activity. For comparative study, apparent rate constants were calculated for all catalyst samples. Since $NaBH_4$ (0.1 mM) was used in excess and which remains almost constant during the reaction progress, pseudo first order kinetics was applied for evaluation of apparent rate constants (k_{app}). The apparent rate constants were calculated from linear plots of $In(A_t/A_0)$ vs reduction time t (Figure 7f). Here A_t and A_0 represents the absorbance of 4-NP after time t = t and t = 0, which can be considered equivalent to concentration at time t = t (C_t) and t = 0 (C_0) respectively. Good linear correlation ($R^2 > 0.98$) of $ln(A_t/A_0)$ vs reduction time was observed for all nanocomposite samples which further confirms the pseudo first order kinetics. The k_{app} values were calculated from slops of linearly fitted plots and entered in Table 3. High catalytic activity was found for all nanocatalyst samples which can be accounted to high electronic conductivity of Ag metal causing fast electron transfer on catalyst surface. The order of rate constants for insitu synthesized RGO nanocomposites from higher to lower is $Ag_{50}Ni_{50}$/RGO > $Ag_{75}Ni_{25}$/RGO > $Ag_{25}Ni_{75}$/RGO > Ag/RGO > bare $Ag_{50}Ni_{50}$. Graphene supported NPs showed better catalytic activity as compared to bare AgNi alloy NPs indicating that catalytic efficiency of AgNi NPs can be enhanced by supporting them on RGO sheets. This type of enhancement in catalytic activity can be attributed to following factors: (1) Π- Π electron interaction property of graphene sheets with organic molecule by which it can hold the substrate molecule, (2) high electronic conductivity of RGO sheets which helps in fast electron transfer rate between substrate molecules by means of active sites of NPs, (3) As compared to bare AgNi NPs it will provide a support for NPs growth and prevent their aggregation. As shown in Table 3, graphene supported Ag_xNi_{100-x} alloy NPs showed higher activity as compared to monometallic Ag NPs which is obviously due to enhancement in electronic properties after mixing electronegatively different Ag and Ni metal atoms. Moreover among different alloy compositions $Ag_{50}Ni_{50}$ alloy NPs have highest rate constant value which may be due to balanced Ag:Ni ratio (i.e. 1:1) leading to best synergistic effect. Elaborating the last point, in present case Ag (1.93) and Ni (1.91) have different electronegativity which may cause electron transfer from Ni to Ag resulting partial charge separation on AgNi alloy surface. This type of charge separation may enhance the catalytic activity of present AgNi/RGO nanocomposites by increased substrate

interaction with catalyst surface. Since this type of synergisms directly depend upon Ag/Ni ratio. The RGO supported $Ag_{50}Ni_{50}$ alloy NPs have balanced Ag/Ni ratio which may causes best charge separation resulting its highest activity among other alloy nanocomposites. The higher activity of $Ag_{75}Ni_{25}$/RGO (Ag/Ni : 3/1) over $Ag_{25}Ni_{75}$/RGO (Ag/Ni : 1/3) can be explained on the basis of larger amount of highly conductive Ag metal causing fast electron transfer on catalyst surface.[29] Furthermore, according to Sabatier principle interaction of substrate and catalyst should be optimum for higher catalytic activity. In present case insitu $Ag_{50}Ni_{50}$/RGO exhibits highest activity which might be due to optimum adsorption desorption behavior of reactants on catalyst surface which is further best for balanced Ag/Ni ratios. To compare present work with earlier literature, rate constants were normalized to weight of catalyst taken and represented in terms of activity parameter $K = k_{app}/m$, where k is rate constant and m is amount of catalyst loaded. The activity parameters of some recently reported different nanocatalysts were compared with present highest active $Ag_{50}Ni_{50}$/RGO nanocomposite (Supplementary Table 1). The RGO supported Ag_xNi_{100-x} nanocatalyst synthesized here exhibits superior catalytic activity over highest values reported till date for same catalytically induced reduction reaction. The exceptionally high catalytic activity of present AgNi alloy NPs can be ascribed to its small size, surfactant free surfaces, enhanced electronic properties and RGO as a support.

For studying the effect of supporting material (activated carbon, SBA-15) and synthesis method (exsitu or insitu), the rate constants were calculated for insitu AgNi/C, insitu AgNi/SBA-15, exsitu AgNi/RGO and exsitu AgNi/C nanocomposites following first order kinetics from linear fitting of ln (A_t/A_0) vs time plots and obtained results were displayed in figure S4a. Since different amount of catalyst was used for studying reaction kinetics so that we calculated activity parameter K for comparison of all these samples. The calculated activity parameters K were compared with insitu synthesized AgNi/RGO nanocomposite and results are in order as, insitu AgNi/RGO (968 $s^{-1}g^{-1}$) > insitu AgNi/C (214 $s^{-1}g^{-1}$) > exsitu AgNi/RGO (97.4 $s^{-1}g^{-1}$) > exsitu AgNi/C (71.9 $s^{-1}g^{-1}$) > insitu AgNi/SBA-15 (11.21 $s^{-1}g^{-1}$). SBA-15 supported nanoparticles showed lowest activity compared to activated carbon or graphene supported NPs which indicated enhancing effect of activated carbon or graphene support in reduction of nitro compounds. This enhancement in activity can be attributed to their Π-Π stacking interaction tendency with organic substrates. Since size of NPs directly affects the catalytic activity so that insitu synthesized AgNi/RGO show highest activity among all supported materials which may be due to its highest

surface area i.e. due to smaller size of AgNi alloy NPs (~11±3 nm), while other supported materials have either bigger (insitu AgNi/C, ~30±3 nm) or aggregated NPs (exsitu AgNi/RGO, exsitu AgNi/C) consequences their lower activity.

The reusability of $Ag_{50}Ni_{50}$/RGO nanocomposites was checked upto four cycles. As shown in Figure 7g-h nanocomposites show excellent recyclability even after four recycling test without any significant loss of catalytic activity. The rate constant calculated for fourth cycle was 0.04623 s^{-1} which is nearer to initial rate constant value indicating good stability of as synthesized $Ag_{50}Ni_{50}$/RGO nanocomposites. For further studying the stability of nanocomposites, we collected the nanocatalyst sample after four catalytic runs and characterized by XRD and TEM analysis. XRD results of used catalyst showed similar pattern as compared to fresh sample indicating excellent stability as expected from a heterogeneous catalyst while from TEM analysis some agglomerations of AgNi alloy NPs were found which may be due to their continuous use resulting slight decrease in catalytic activity after 4th cycle (Figure S5). High recycling stability for Ag_xNi_{100-x}/RGO nanocomposites indicates perfect interaction between RGO nanosheets and Ag_xNi_{100-x} alloy NPs.

Apart from 4-NP, highest active $Ag_{50}Ni_{50}$/RGO nanocomposites were applied in reduction of other nitro-aromatic compounds. Similar reaction scheme (as followed in 4-NP reduction) was applied for all nitro compounds and progress of reaction was again monitored by UV-Vis absorption spectroscopy. The absorption spectra for ANP, 4-NA, 2-NP, 2-NA, 3-NA and FNA were shown in Figure 8a-f respectively which display very fast reduction of present nitro-compounds using only 0.05 mg of $Ag_{50}Ni_{50}$/RGO nanocomposites. The apparent rate constant k_{app} and activity parameter K were calculated for all nitro-aromatic compounds by applying pseudo first order kinetics and data was entered in Table 4 (figure 8g). As obtained activity parameters are best as compared to earlier literature for catalytic reduction for similar nitro compounds. These excellent results again represent the exceptional catalytic activity for present Ag_xNi_{100-x}/RGO nanocomposites. Recently AB has been found as potential reducing agent in tandem reduction of nitro-aromatic compounds.[44] Hence to extend this approach of tandem reactions, we have applied AB as a tandem reducing agent and the reaction kinetics of all nitro derivatives was studied. Here, reaction condition was not kept similar to NaBH$_4$ induced reduction reactions because insitu $Ag_{50}Ni_{50}$/RGO showed very slow hydrolysis of ammonia borane without stirring. In all tandem reduction reactions, concentration of ammonia borane were

kept higher compared to nitro compounds and first order kinetics was applied. The rate constants were calculated for all tandem reactions from linear fitting of ln (A_t/A_0) vs time plots and obtained results were entered in table 4. Figure S4b display the first order kinetics plots for all tandem reduction reactions. Since we have varied the amount of substrates and catalysts in tandem reactions, hence for comparison of obtained results with $NaBH_4$ induced reactions, activity parameters were calculated for all tandem reactions and obtained data were entered in table 4. Here, $Ag_{50}Ni_{50}$/RGO nanocomposites showed high activity towards tandem reduction of nitro compounds but obtained activity parameters were less as compared to $NaBH_4$ induced reduction reactions which is due to comparable slower hydrogen generation capacity of nanocatalyst with ammonia borane complex.

Conclusions

In summary, Ag_xNi_{100-x} alloy nanoparticles with different compositions were successfully grown on RGO nanosheets using one pot, wet chemical co-reduction technique. As demonstrated in AgNi/RGO nanocomposites, the aspect ratio and composition could be easily controlled by simply varying the Ag/Ni precursor ratio. The Ag_xNi_{100-x} alloy NPs are homogeneously distributed on RGO sheets with narrow size distribution and exhibit weak ferromagnetic properties. In addition, nanocomposites show composition dependent excellent catalytic activity and stability towards 4-NP reduction with exceptionally high rate constants and activity parameters. Similarly these nanocomposites also show overwhelming catalytic activity towards reduction of other nitro derivatives. The novel Ag_xNi_{100-x} nanocomposites are easy to synthesize, cost effective, exceptionally active and reusable which make it a possible candidate for various practical applications in industries.

Electronic supplementary information (ESI) available: XRD spectra for $Ag_{25}Ni_{75}$/RGO, Ni/RGO, insitu $Ag_{50}Ni_{50}$/C and insitu $Ag_{50}Ni_{50}$/SBA-15 samples. Low resolution TEM images, EDS analysis for $Ag_{25}Ni_{75}$/RGO, $Ag_{75}Ni_{25}$/RGO sample, plots of $ln(A_t/A_0)$ versus time for rate constant calculation for nanocomposite samples and tandem reduction reactions, XRD spectrum and low resolution TEM of used insitu $Ag_{50}Ni_{50}$/RGO nanocatalyst and table for comparative activity of present catalyst with earlier literature.

AUTHOR INFORMATION

Corresponding Author

* E-mail: kidwai.chemistry@gmail.com, Fax: (91-11) 27666235

References

1. C. N. R. Rao, A. K. Sood, K. S. Subrahmanyam and A. Govindaraj, *Angewandte Chemie International Edition*, 2009, **48**, 7752-7777.

2. A. K. Geim and K. S. Novoselov, *Nat Mater*, 2007, **6**, 183-191.

3. A. Peigney, C. Laurent, E. Flahaut, R. R. Bacsa and A. Rousset, *Carbon*, 2001, **39**, 507-514.

4. J. C Reed, H. Zhu, A. Y. Zhu, C. Li, and E. Cubukcu, *Nano Lett.*, 2012, ***12*,** 4090–4094.

5. L. Britnell, R. V. Gorbachev, R. Jalil, B. D. Belle, F. Schedin, A. Mishchenko, T. Georgiou, M. I. Katsnelson, L. Eaves, S. V. Morozov, N. M. R. Peres, J. Leist, A. K. Geim, K. S. Novoselov and L. A. Ponomarenko, *Science*, 2012, **335**, 947-950.

6. X. Zhu, Y. Zhu, S. Murali, M. D. Stoller and R. S. Ruoff, *ACS Nano*, 2011, **5**, 3333-3338.

7. H. Zhang, X. Lv, Y. Li, Y. Wang and J. Li, *ACS Nano*, 2010, **4**, 380-386.

8. D. C. Marcano, D. V. Kosynkin, J. M. Berlin, A. Sinitskii, Z. Sun, A. Slesarev, L. B. Alemany, W. Lu and J. M. Tour, *ACS Nano*, 2010, **4**, 4806-4814.

9. J. Li, C.-y. Liu and Y. Liu, *Journal of Materials Chemistry*, 2012, **22**, 8426-8430.

10. Z. Ji, X. Shen, G. Zhu, H. Zhou and A. Yuan, *Journal of Materials Chemistry*, 2012, **22**, 3471-3477.

11. T. Zeng, X.-l. Zhang, Y.-r. Ma, H.-y. Niu and Y.-q. Cai, *Journal of Materials Chemistry*, 2012, **22**, 18658-18663.

12. A. Devadoss, P. Sudhagar, S. Das, S. Y. Lee, C. Terashima, K. Nakata, A. Fujishima, W. Choi, Y. S. Kang and U. Paik, *ACS Applied Materials & Interfaces*, 2014, **6**, 4864-4871.

13. Y. Si and E. T. Samulski, *Chemistry of Materials*, 2008, **20**, 6792-6797.

14. M. Kidwai, V. Bansal, A. Kumar, S. Mozumdar, *Green Chemistry,* 2007, **9**, 742-745.

15. M. Kidwai, N. K. Mishra, S. Bhardwaj, A. Jahan, A. Kumar and S. Mozumdar, *ChemCatChem*, 2010, **2**, 1312-1317.

16. Z. Yue, F. Lisdat, W. J. Parak, S. G. Hickey, L. Tu, N. Sabir, D. Dorfs and N. C. Bigall, *ACS Applied Materials & Interfaces*, 2013, **5**, 2800-2814.

17. J. Xiao and S. Yang, *Journal of Materials Chemistry*, 2012, **22**, 12253-12262.

18. G. Chen, S. Desinan, R. Nechache, R. Rosei, F. Rosei and D. Ma, *Chemical Communications*, 2011, **47**, 6308-6310.

19. S. Senapati, S. K. Srivastava, S. B. Singh, H. N. Mishra, *Journal of Materials Chemistry*, 2012, **22**, 6899-6906.

20. J. Guo, X. Wang, P. Miao, X. Liao, W. Zhang and B. Shi, *Journal of Materials Chemistry*, 2012, **22**, 11933-11942.

21. M. B. Gawande, H. Guo, A. K. Rathi, P. S. Branco, Y. Chen, R. S. Varma and D.-L. Peng, *RSC Advances*, 2013, **3**, 1050-1054.

22. E. Ma, *Progress in Materials Science*, 2005, **50**, 413-509.

23. C.-Y. Tung, J. M. Gu, H.-M. Lin, Y. Hwu and N.-F. Cheng, *Nanostructured Materials*, 1997, **9**, 351-354.

24. Z. Zhang, T. M. Nenoff, J. Y. Huang, D. T. Berry and P. P. Provencio, *The Journal of Physical Chemistry C*, 2009, **113**, 1155-1159.

25. Z. Zhang, T. M. Nenoff, K. Leung, S. R. Ferreira, J. Y. Huang, D. T. Berry, P. P. Provencio and R. Stumpf, *The Journal of Physical Chemistry C*, 2010, **114**, 14309-14318.

26. C. Srivastava, S. Chithra, K. D. Malviya, S. K. Sinha and K. Chattopadhyay, *Acta Materialia*, 2011, **59**, 6501-6509.

27. K. Santhi, E. Thirumal, S. N. Karthick, H.-J. Kim, M. Nidhin, V. Narayanan and A. Stephen, *J Nanopart Res*, 2012, **14**, 1-12.

28. K. Sridharan, T. Endo, S.-G. Cho, J. Kim, T. J. Park and R. Philip, *Optical Materials*, 2013, **35**, 860-867.

29. M. Kumar and S. Deka, *ACS Applied Materials & Interfaces*, 2014, **6**, 16071-16081.

30. M. E. DeLorenzo, G. I. Scott and P. E. Ross, *Environmental Toxicology and Chemistry*, 2001, **20**, 84-98.

31. M. Megharaj, H. W. Pearson and K. Venkateswarlu, *Arch. Environ. Contam. Toxicol.*, 1991, **21**, 578-584.

32. Y. Xu, H. Bai, G. Lu, C. Li and G. Shi, *Journal of the American Chemical Society*, 2008, **130**, 5856-5857.

33. F. Tuinstra and J.L. Koenig, J. Chem. Phys., 1970, **53**, 1126.

34. S. Bai, X. Shen, G. Zhu, M. Li, H. Xi, and K. Chen, *ACS Applied Materials & Interfaces*, 2012, **4**, 2378-2386.

35. S. K. Bhunia and N. R. Jana, *ACS Applied Materials & Interfaces*, 2014, **6**, 20085-20092.

36. S. Saha, A. Pal, S. Kundu, S. Basu and T. Pal, *Langmuir*, 2010, **26**, 2885-2893.

37. J. Yang, X. Shen, G. Zhu, Z. Ji and H. Zhou, *RSC Adv.*, 2014, **4**, 386.

38. J. Huang, S. Vongehr, S. Tang, H. Lu, and X. Meng, *J. Phys. Chem.* C, 2010, **114**, 15005–15010.

39. H. Fu, X. Yang, X. Jiang, and A. Yu, *Langmuir*, 2013, **29**, 7134−7142.

40. F.–h. Lin and R.-a. Doong, *J. Phys. Chem. C*, 2011, **115**, 6591–6598.

41. Y. Zhu, J. Shen, K. Zhou, C. Chen, X. Yang, and C. Li, *J. Phys. Chem. C*, 2011, **115**, 1614–1619.

42. Y.-Y. Shen, Y. Sun, L.-N. Zhou, Y.-J. Li and E. S. Yeung, *J. Mater. Chem. A*, 2014, **2**, 2977–2984.

43. J. Zhang, G. Chen, D. Guay, M. Chaker and D. Ma, *Nanoscale*, 2014, **6**, 2125.

44. H. Goksu, S. F. Ho, O. Metin, K. Korkmaz, A. M. Garcia, M. S. Gultekin and S.Sun, *ACS Catal.*, 2014, **4**, 1777-1782.
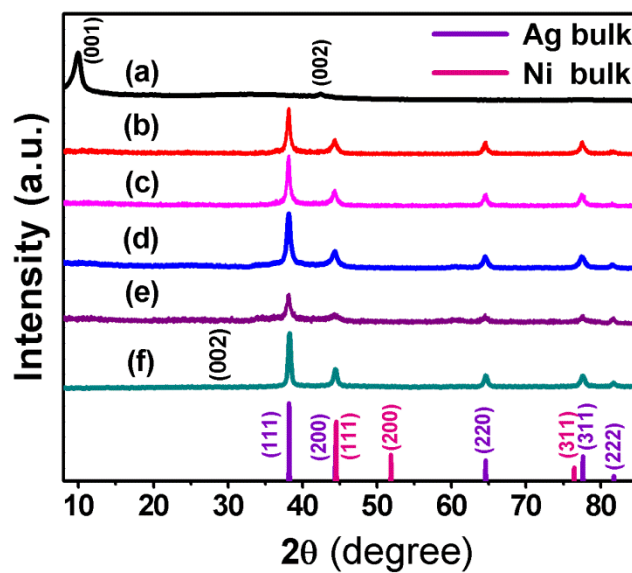
Figure 1. XRD pattern of synthesized (a) GO, (b) Ag/RGO, (c) $Ag_{75}Ni_{25}$/RGO, (d) $Ag_{50}Ni_{50}$/RGO, (e) $Ag_{25}Ni_{75}$/RGO nanocomposites and (f) bare $Ag_{50}Ni_{50}$ alloy NPs. (At bottom standard XRD pattern for bulk Ag in violet and Ni in pink).
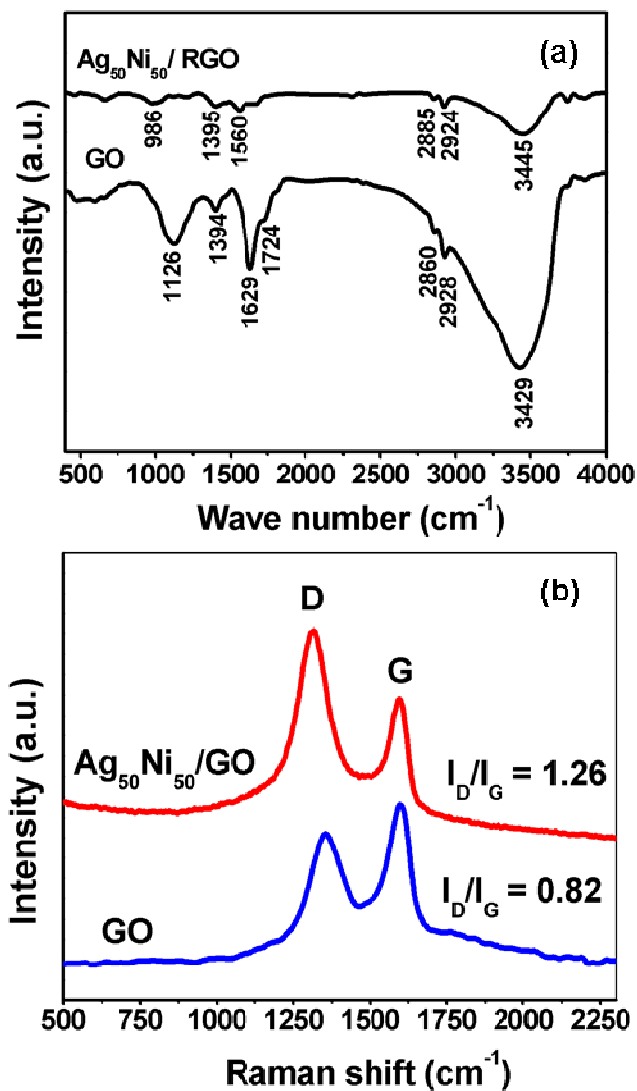
Figure 2. (a) FTIR and (b) RAMAN spectra for GO and $Ag_{50}Ni_{50}$/RGO nanocomposite samples.
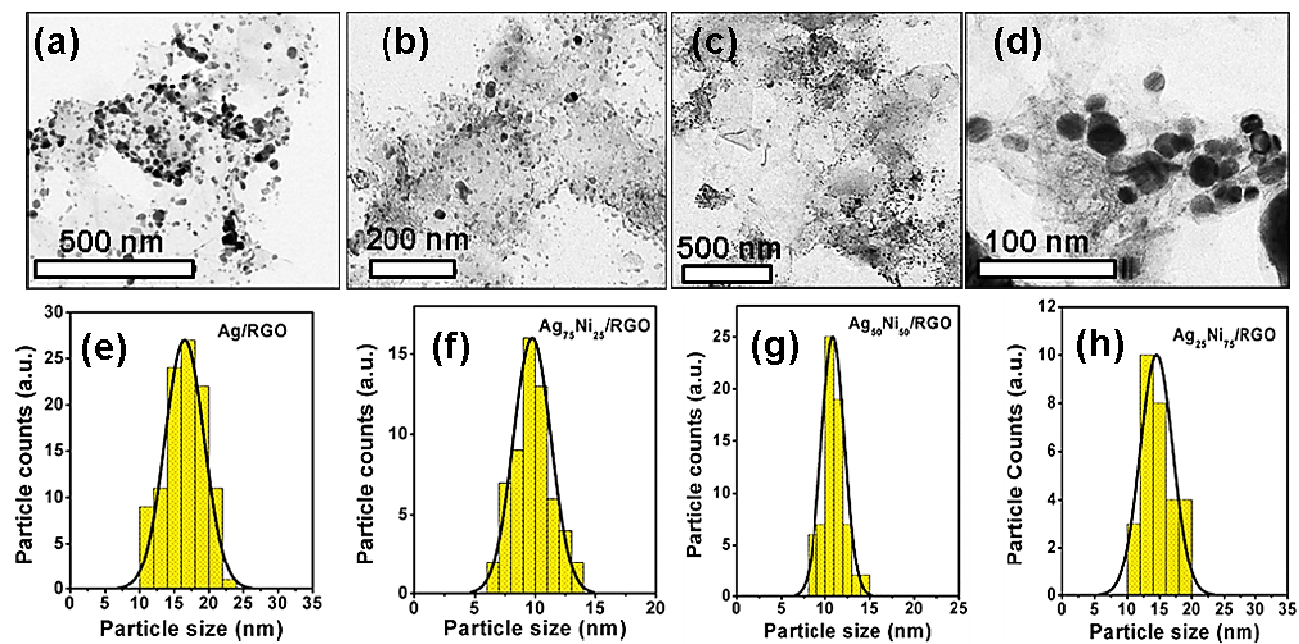
Figure 3. Low resolution TEM images for (a) Ag/RGO, (b) Ag$_{75}$Ni$_{25}$/RGO, (c) Ag$_{50}$Ni$_{50}$/RGO and (d) Ag$_{25}$Ni$_{75}$/RGO samples. Histogram showing particle size disribution for as synthesized (a) Ag/RGO, (b) Ag$_{75}$Ni$_{25}$/RGO, (c) Ag$_{50}$Ni$_{50}$/RGO and (d) Ag$_{25}$Ni$_{75}$/RGO samples.
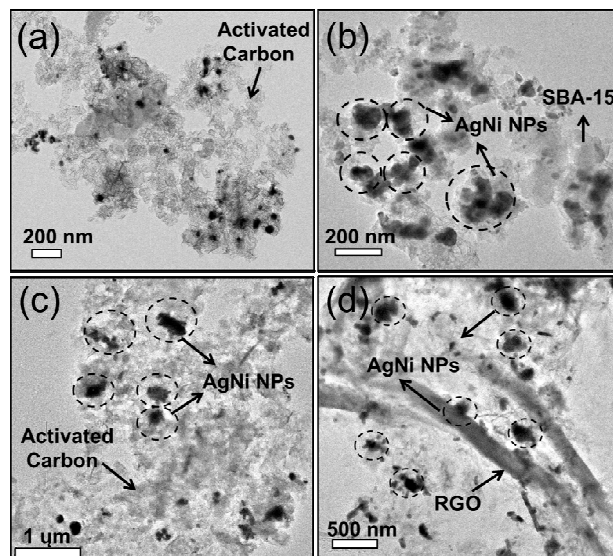
Figure 4. Low resolution TEM images of (a) insitu $Ag_{50}Ni_{50}$/C, (b) insitu $Ag_{50}Ni_{50}$/SBA-15, (c) exsitu $Ag_{50}Ni_{50}$/C and (d) exsitu $Ag_{50}Ni_{50}$/RGO nanocomposites.
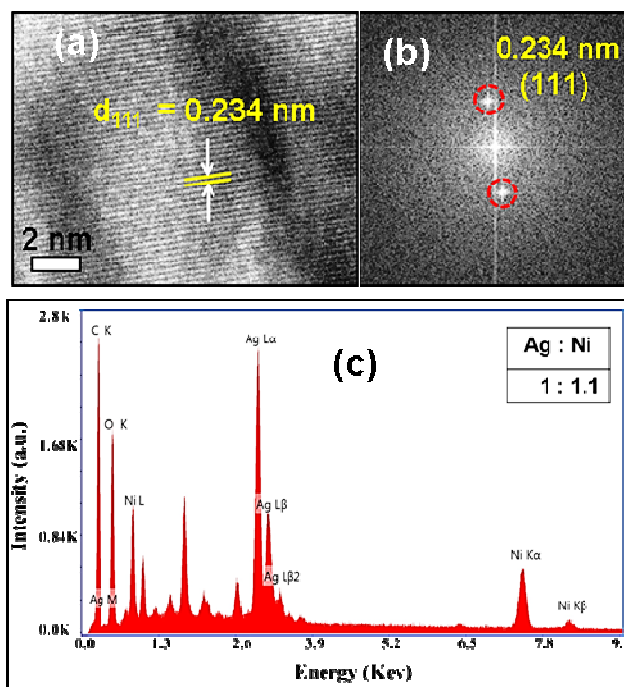
Figure 5. (a) High resolution TEM image, (b) calculated 2D-FFT image for region shown in panel 'a', (c) SEM-EDAX analysis for $Ag_{50}Ni_{50}$/RGO nanocomposite sample (Atomic ratio of Ag/Ni in table) .
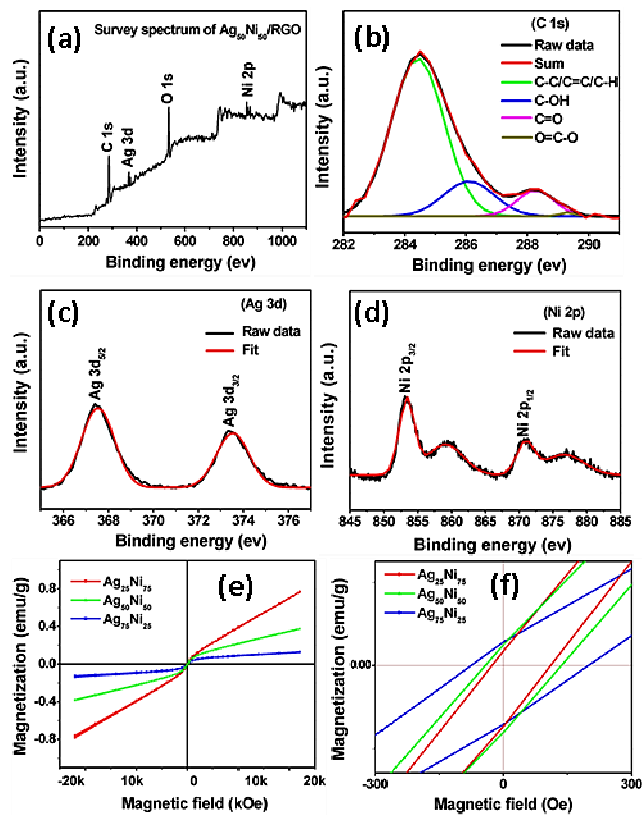
Figure 6. (a) Wide scan XPS spectrum for $Ag_{50}Ni_{50}$/RGO, high resolution XPS for (b) C 1s, (c) Ag 3d and (d) Ni 2p. (e) Magnetic hysteresis loops for Ag_xNi_{100-x}/RGO samples, (f) magnified hysteresis loops of region shown in panel 'e'.
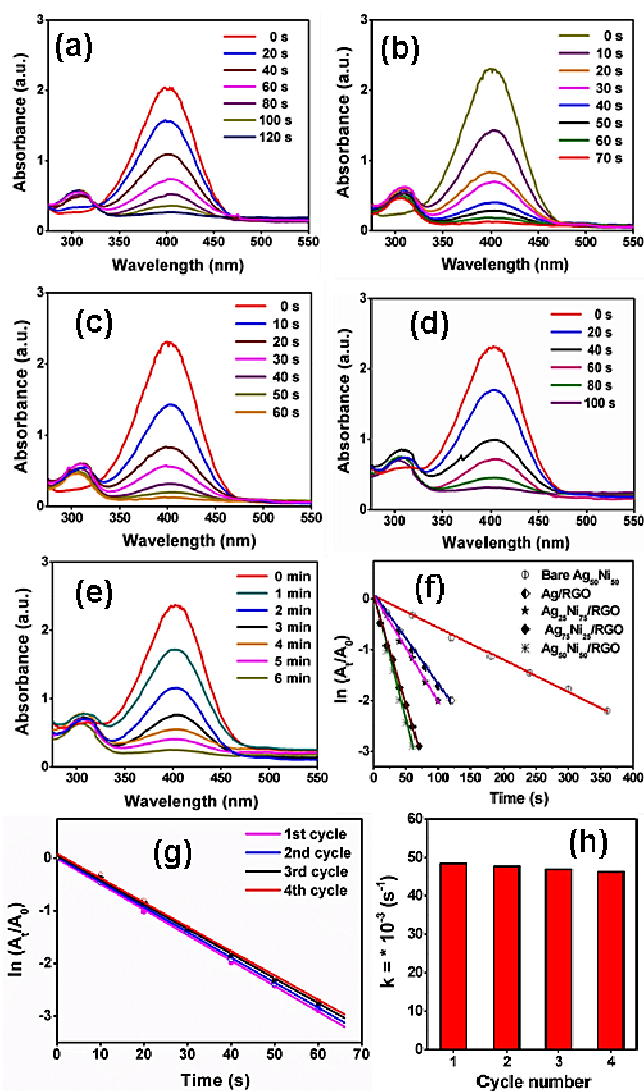
Figure 7. UV-Vis absorption spectra for reduction of 4-NP by $NaBH_4$ in presence of (a) Ag/RGO, (b) $Ag_{75}Ni_{25}$/RGO, (c) $Ag_{50}Ni_{50}$/RGO, (d) $Ag_{25}Ni_{75}$/RGO and (e) bare $Ag_{50}Ni_{50}$. (f) Plots of $In(A_t/A_0)$ versus time for rate constant calculation of as synthesized samples. (g) Plots of $In(A_t/A_0)$ versus reduction time showing reusability of highest active $Ag_{50}Ni_{50}$/RGO sample for 4-NP reduction, (h) value of k_{app} for each succusive cycle using $Ag_{50}Ni_{50}$/RGO sample.

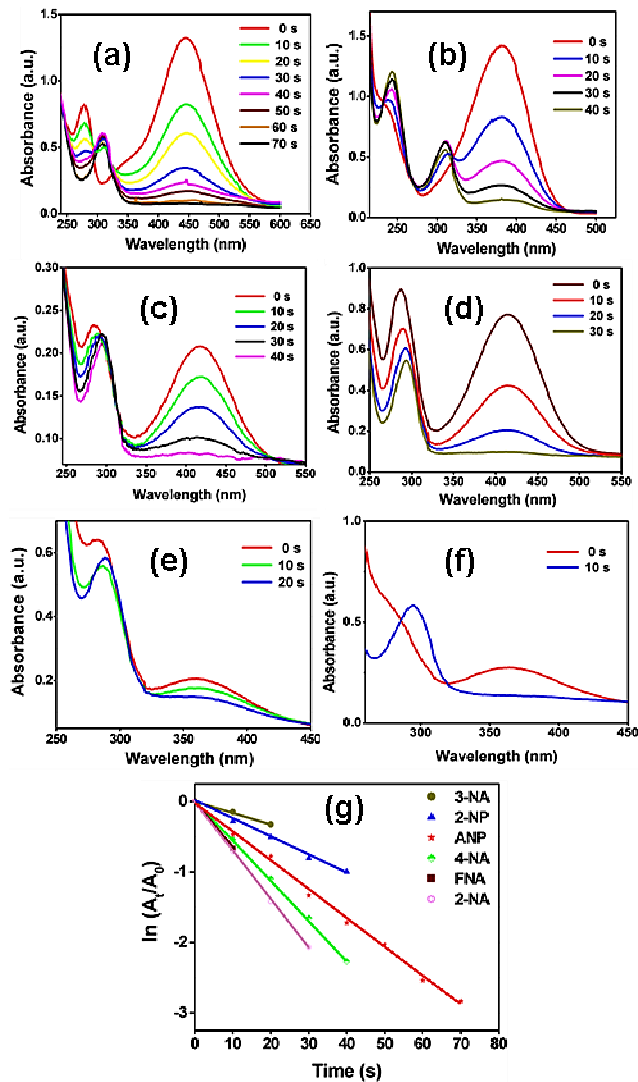**Figure 8.** UV-Vis absorption spectra for reduction of (a) ANP, (b) 4-NA, (c) 2-NP, (d) 2-NA, (e) 3-NA and (f) FNA using $Ag_{50}Ni_{50}$/RGO nanocomposites. (g) Plots of $In(A_t/A_0)$ versus reduction time using highest active $Ag_{50}Ni_{50}$/RGO sample.

Table 1. Sample of Ag_xNi_{100-x} nanocomposites with various initial precursor molar ratio and corresponding ICP-AES results.

Samples	Precursor amount (mmol)	Ag/Ni molar ratio (ICP)	% Loading (ICP)
Ag/RGO	$Ag^+ = 0.3$	-	-
$Ag_{75}Ni_{25}$/RGO	$Ag^+ (0.225) + Ni^{2+} (0.075) = 0.3$	2.95:1	28.30
$Ag_{50}Ni_{50}$/RGO	$Ag^+ (0.15) + Ni^{2+} (0.15) = 0.3$	1:1.1	25.59
$Ag_{25}Ni_{75}$/RGO	$Ag^+ (0.075) + Ni^{2+} (0.225) = 0.3$	1:2.93	28.71
$Ag_{50}Ni_{50}$	$Ag^+ (0.15) + Ni^{2+} (0.15) = 0.3$	-	-

Table 2. Saturation magnetization (M_S), Remanent magnetization (M_r) and Coercivity (H_C), values for various Ag_xNi_{100-x}/RGO nanocomposites.

Nanocomposite sample	M_S (emu/g)	M_r (emu/g)	H_C (Oe)
$Ag_{25}Ni_{75}$/RGO	0.771	0.0025	24.575
$Ag_{50}Ni_{50}$/RGO	0.378	0.0036	44.052
$Ag_{75}Ni_{25}$/RGO	0.124	0.0042	75.555

Table 3. The correlation coefficient of $\ln(A_t/A_0)$ vs t plot, reduction time, apparent rate constant and activity parameter for reduction of 4-NP with $NaBH_4$ in presence of Ag_xNi_{100-x}/RGO nanocomposites and bare $Ag_{50}Ni_{50}$ alloy NPs.

Nanocatalyst sample	R^2	Reduction time (s)	k_{app} ($\times10^{-3}$ sec^{-1})	$K = s^{-1}g^{-1}$
Ag/RGO	0.99910	120	17.15	343
$Ag_{75}Ni_{25}$/RGO	0.99892	70	41.09	821.8
$Ag_{50}Ni_{50}$/RGO	0.99946	60	48.40	968
$Ag_{25}Ni_{75}$/RGO	0.99852	100	20.68	413.6
Bare $Ag_{50}Ni_{50}$	0.99889	360	6.07	121.4

Table 4. The correlation coefficient of $\ln(A_t/A_0)$ vs t plot, reduction time, apparent rate constant and activity parameter for reduction of various nitroarenes with $NaBH_4$ in presence of highest active $Ag_{50}Ni_{50}$/RGO nanocomposite.

Sample name	R^2	Reduction time (s)	k_{app} ($NaBH_4$) ($\times10^{-3}$ sec^{-1})	k_{app} (AB) ($\times10^{-3}$ sec^{-1})	$K = s^{-1}g^{-1}$ ($NaBH_4$)	$K = s^{-1}g^{-1}$ (AB)
ANP	0.998	70	40.86	1.49	817.2	2.98
4-NA	0.999	40	56.49	3.09	1129.8	6.18
2-NP	0.998	40	25.25	11.5	505.0	23
2-NA	0.999	30	69.09	2.69	1381.8	5.38
3-NA	0.998	20	16.34	17.9	326.8	35.9
FNA	1	10	66.81	6.40	1336.2	12.8
4-NP	0.999	60	48.4	3.18	968	6.36

GRAPHICAL ABSTRACT

Use of RGO supported Ag_xNi_{100-x} alloy nanoparticles in reduction of nitroarenes showing high activity and stability.